1

Thermodynamic properties of nano-silver and alloy particles

Wangyu Hu, Shifang Xiao, Huiqiu Deng, Wenhua Luo and Lei Deng
Department of Applied Physics, Hunan University, Changsha 410082, PR China

In this chapter, the analytical embedded atom method and calculating Gibbs free energy method are introduced briefly. Combining these methods with molecular dynamic and Monte Carlo techniques, thermodynamics of nano-silver and alloy particles have been studied systematically.

For silver nanoparticles, calculations for melting temperature, molar heat of fusion, molar entropy of fusion, and temperature dependences of entropy and specific heat capacity indicate that these thermodynamic properties can be divided into two parts: bulk quantity and surface quantity, and surface atoms are dominant for the size effect on the thermodynamic properties of nanoparticles.

Isothermal grain growth behaviors of nanocrystalline Ag shows that the small grain size and high temperature accelerate the grain growth. The grain growth processes of nanocrystalline Ag are well characterized by a power-law growth curve, followed by a linear relaxation stage. Beside grain boundary migration and grain rotation mechanisms, the dislocations serve as the intermediate role in the grain growth process. The isothermal melting in nanocrystalline Ag and crystallization from supercooled liquid indicate that melting at a fixed temperature in nanocrystalline materials is a continuous process, which originates from the grain boundary network. The crystallization from supercooled liquid is characterized by three characteristic stages: nucleation, rapid growth of nucleus, and slow structural relaxation. The homogeneous nucleation occurs at a larger supercooling temperature, which has an important effect on the process of crystallization and the subsequent crystalline texture. The kinetics of transition from liquid to solid is well described by the Johnson-Mehl-Avrami equation.

By extrapolating the mean grain size of nanocrystal to an infinitesimal value, we have obtained amorphous model from Voronoi construction. From nanocrystal to amorphous state, the curve of melting temperature exhibits three characteristic regions. As mean grain size above about 3.8 nm for Ag, the melting temperatures decrease linearly with the reciprocal of grain size. With further decreasing grain size, the melting temperatures almost keep a constant. This is because the dominant factor on melting temperature of nanocrystal shifts from grain phase to grain boundary one. As a result of fundamental difference in structure, the amorphous has a much lower solid-to-liquid transformation temperature than that of nanocrystal.

The surface and size effects on the alloying ability and phase stability of Ag alloy nanoparticles indicated that, besides the similar compositional dependence of heat of formation as in bulk alloys, the heat of formation of alloy nanoparticles exhibits notable size-dependence, and there exists a competition between size effect and compositional effect on the heat of formation of alloy system. Contrary to the positive heat of formation for bulk immiscible alloys, a negative heat of formation may be obtained for the alloy nanoparticles with a small size or dilute solute component, which implies a promotion of the alloying ability and phase stability of immiscible system on a nanoscale. The surface segregation results in an extension of the size range of particles with a negative heat of formation.

1. Thermodynamic properties of silver nanoparticles

Nanoparticle systems currently attract considerable interest from both academia and industry because of their interesting and diverse properties, which deviate from those of the bulk. Owing to the change of the properties, the fabrication of nanostructural materials and devices with unique properties in atomic scale has become an emerging interdisciplinary field involving solid-state physics, chemistry, biology, and materials science. Understanding and predicting the thermodynamics of nanoparticles is desired for fabricating the materials for practical applications.[1] The most striking example of the deviation of the corresponding conventional bulk thermodynamic behavior is probably the depression of the melting point of small particles of metallic species. A relation between the radius of nanoparticles and melting temperature was first established by Pawlow,[2] and the first experimental investigation of melting-temperature dependence on particle size was conducted more than 50 years ago.[3] Further studies were performed by a great number of researchers.[4-12] The results reveal that isolated nanoparticles and substrate-supported nanoparticles with relatively free surfaces usually exhibit a significant decrease in melting temperature as compared with the corresponding conventional bulk materials. The physical origin for this phenomenon is that the ratio of the number of surface-to-volume atoms is enormous, and the liquid/vapor interface energy is generally lower than the average solid/vapor interface energy.[9] Therefore, as the particle size decreases, its surface-to-volume atom ratio increases and the melting temperature decreases as a consequence of the improved free energy at the particle surface.

A lot of thermodynamic models of nanoparticles melting assume spherical particles with homogeneous surfaces and yield a linear or almost linear decreasing melting point with increasing the inverse of the cluster diameter.[2,6,10-12] However, the determination of some parameters in these models is difficult or arbitrary. Actually, the melting-phase transition is one of the most fundamental physical processes. The crystal and liquid phases of a substance can coexist in equilibrium at a certain temperature, at which the Gibbs free energies of these two phases become the same. The crystal phase has lower free energy at a temperature below the melting point and is the stable phase. As the temperature goes above the melting point, the free energy of the crystal phase becomes higher than that of the liquid phase and phase transition will take place. The same holds true for nanoparticles. We have calculated the Gibbs free energies of solid and liquid phases for silver bulk material and its surface free energy using molecular dynamics with the modified analytic embedded-atom method (MAEAM). By representing the total Gibbs free energies of solid and liquid clusters as the sum of the central bulk and surface free energy,[5,13,14] we can attain the free energies

for the liquid and solid phase in spherical particles as a function of temperature. The melting temperature of nanoparticles is obtained from the intersection of these free-energy curves. This permits us to characterize the thermodynamic effect of the surface atoms on size-dependent melting of nanoparticles and go beyond the usual phenomenological modeling of the thermodynamics of melting processes in nanometer-sized systems. In addition, we further calculate the molar heat of fusion, molar entropy of fusion, entropy, and specific heat capacity of silver nanoparticles based on free energy calculation.

In order to explore the size effect on the thermodynamic properties of silver nanoparticles, we first write the total Gibbs free energy G^{total} of a nanoparticle as the sum of the volume free energy G^{bulk} and the surface free energy G^{surface}

$$G^{total} = G^{bulk} + G^{surface} = Ng(T) + \gamma(T)A_s \tag{1}$$

The detailed description on calculation of G^{bulk} and G^{surface} has been given in Ref. 15-17. Assuming a spherical particle leads to a specific surface area of[5,10,18]

$$A_s = \frac{6}{D} N v_{at}(T) \tag{2}$$

where N is the total number of atoms in the particle, D is the radius of the particle, and $v_{at}(T)$ is the volume per atom. Second-order polynomials are adjusted to the simulation results of the internal energy for the solid and liquid phase shown in Fig. 1. The Gibbs free energies per atom for the solid and liquid phase are written as

$$\begin{aligned} g(T) = g(T_0)(T/T_0) - T[a_2(T-T_0) + a_1 \ln(T/T_0) \\ - a_0(1/T - 1/T_0)] \end{aligned} \tag{3}$$

where a_i are the polynomial coefficients, resulting from molecular dynamics (MD) simulations.[17]

The surface free energy of a solid spherical particle may be determined by the average surface free energy of the crystallite facets and the Gibbs−Wulff relation[19]

$$\sum_i A_i \gamma_{si} = \text{mininum} \tag{4}$$

The equilibrium crystal form develops so that the crystal is bound by low surface energy faces in order to minimize the total surface free energy.[20] For two surfaces i and j at equilibrium, $A_i\gamma_i = A_j\gamma_j = \mu$, where μ is the excess chemical potential of surface atoms relative to interior atoms. A surface with higher surface free energy (γ_i) consequently has a smaller surface area (A_i), which is inversely proportional to the surface free energy. Accordingly, the average surface free energy of the crystal, weighted by the surface area, is

$$\gamma_S = \frac{\sum_{i=1}^{n} A_i \gamma_{si}}{\sum_{i=1}^{n} A_i} = \frac{\sum_{i=1}^{n} \frac{\mu}{\gamma_i} \gamma_{si}}{\sum_{i=1}^{n} \frac{\mu}{\gamma_{si}}} = \frac{n}{\sum_{i=1}^{n} \frac{1}{\gamma_{si}}} \tag{5}$$

where n is the number of facets under consideration. Each crystal has its own surface energy, and a crystal can be bound by an infinite number of surface types. Thus, we only consider three low index surfaces, (111), (100), and (110), because of their low surface energies, and the surface free energy γ_i of the facet i is calculated as follows

$$\gamma_i(T) = \gamma_i(T_0)\frac{T}{T_0} - T[b_{2i}(T - T_0) + b_{1i} \ln(\frac{T}{T_0}) - \frac{b_{0i}}{T} + \frac{b_{0i}}{T_0}] \tag{6}$$

where b_{ki} (k = 0,1,2) are the coefficients for the surface free-energy calculation for facet i, and

$\gamma_i(T_0)$ is surface free energy at the reference temperature T_0.[17] On the basis of the expression for the Gibbs free energy, general trends for thermodynamic properties may be deduced. For example, the melting temperature T_m for nanoparticles of diameter D can be obtained by equating the Gibbs free energy of solid and liquid spherical particles with the assumption of constant pressure conditions, and temperature and particle size dependence of the entropy per atom for solid nanoparticles can then be defined using the following expression

$$\begin{aligned} s^s(T,D) &= -(\frac{\partial g^s}{\partial T})_p \\ &= 2a_2{}^sT + a_1{}^s\ln(\frac{T}{T_0}) - \frac{g^s(T_0)}{T_0} - a_2{}^sT_0 + a_1{}^s + \frac{a_0{}^1}{T_0} - \frac{2v_{at}(T)\,(\gamma^s)^2}{D}\sum_{i=1}^{3}\frac{\gamma_i^{'}}{\gamma_i^2} \end{aligned} \tag{7}$$

where the primes denote derivatives with regard to temperature. The contribution from the derivative of atomic volume is trivial; it is reasonable to neglect. Using the relation between the specific heat capacity at constant pressure and the entropy, we can write the expression for the specific heat capacity per mole as

$$\begin{aligned} C_p^s(T,D) &= N_0T(\frac{\partial s^s}{\partial T})_p \\ &= 2N_0a_2^sT + N_0a_1^s - \frac{6N_0Tv_{at}(T)}{D}\left\{\frac{2}{\gamma^s}[(\gamma^s)^{'}]^2 + \frac{(\gamma^s)^2}{3}\sum_{i=1}^{3}\left[\frac{\gamma_i^{''}}{\gamma_i^2} - \frac{2(\gamma_i^{'})^2}{\gamma_i^3}\right]\right\} \end{aligned} \tag{8}$$

where N_0 is Avogadro's number. The internal energy per atom for nanoparticles can be written as[5,10]

$$h_{v,D}(T,D) = h_v(T) + \frac{6v_{at}(T)\;\gamma(T)}{D} \tag{9}$$

where h_v represents the internal energy per atom of bulk material. The molar heat of fusion and molar entropy of fusion for nanoparticles can be derived from the internal energy difference of solid and liquid nanoparticles easily.

$$\begin{aligned} \Delta H_m &= N_0\left[h_{v,D}^l(T_m,D) - h_{v,D}^s(T_m,D)\right] \\ &= \Delta H_{mb}\left[1 - \frac{6v_{at}^s(T_m)}{LD}(\gamma^s(T_m) - \gamma^l(T_m)\frac{v_{at}^l(T_m)}{v_{at}^s(T_m)})\right] \\ &= \Delta H_{mb}\left[1 - \frac{\beta_1(T_m)}{D}\right] \end{aligned} \tag{10}$$

where ΔH_{mb} is the molar heat of fusion for bulk, and L is the latent heat of melting per atom. The superscript "s" and "l" represent solid phase and liquid phase, respectively.

Figure 1 shows the behavior of the solid and liquid internal enthalpies as a function of temperature, and an abrupt jump in the internal energy during heating can be observed, but this step does not reflect the thermodynamic melting because periodic boundary condition calculations provide no heterogeneous nucleation site, such as free surface or the solid-liquid interface, for bulk material leading to an abrupt homogeneous melting transition at about 1500 K (experimental melting point 1234 K), as it is revealed that the confined lattice without free surfaces can be significantly superheated.[21] The latent heat of fusion is 0.115 eV/atom, in good agreement with the experimental value of 0.124 eV/atom.[22]

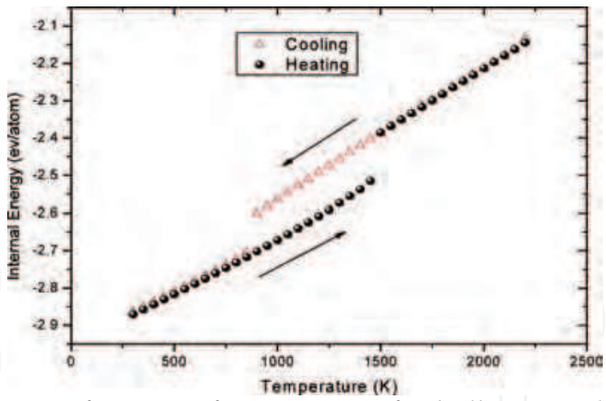

Fig. 1. Internal energy as a function of temperature for bulk material. Heating and cooling runs are indicated by the arrows and symbols. (Picture redrawn from Ref. 17)

The free-energy functions for the solid and liquid phases have been plotted in Fig. 2. The melting temperature T_{mb} is obtained from the intersection of these curves. From Fig. 2, two curves cross at T_{mb}=1243 K, which is in good agreement with the experimental melting point T^{exp} =1234 K. The good agreement in melting point is consistent with accurate prediction of the Gibbs free energies.

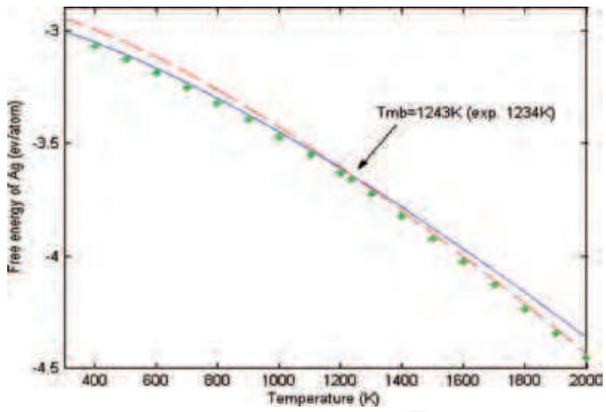

Fig. 2. Gibbs free energy of the solid and liquid phase in units of eV/atom. The asterisks denote the experimental values [22]. The solid curve is the MAEAM solid free energy, and the dashed curve is the MAEAM liquid free energy. The temperature at which Gibbs free energy of the solid and liquid phase is identical is identified as the melting point. (Picture redrawn from Ref. 17)

The calculation results of solid surface free energy for the (111), (100), and (110) surfaces with thermodynamic integration approach (TI)[23] is depicted in Fig. 3. It can be seen that the free energies of the surfaces at low temperatures are ordered precisely as expected from packing of the atoms in the layers. The close-packed (111) surface has the lowest free energy, and loosely packed (110) the largest. As temperature increases, the anisotropy of the surface free energy becomes lower and lower because the crystal slowly disorders. For comparison, we also utilize Grochola et al's "simple lambda" and "blanket lambda" path (BLP)[24,25] to calculate the solid surface free energy for the three low-index faces. The results are in good

agreement with the TI calculation for temperature from 300 to 750 K. As an example, the simulation results for the integrand $<\partial E(\lambda)/\partial\lambda>\lambda + <\partial\varphi_{rep}^{AB}/\partial\lambda>\lambda$ for the (110) face at 750 K is shown in Fig. 4. It is obvious that the results are very smooth and completely reversible. In order to create the slab, we also show the expansion process using z-density plots for $(L_z-L_z^0)/L_z^0$ = 0, 0.045, and 0.08, in Fig. 5. At $(L_z-L_z^0)/L_z^0$=0.08, the adatoms appearing between A and B sides can be seen. According to Grochola et al.,[25] it indicates that the BLP samples the rare events more efficiently than the cleaving lambda method [26] because the two surfaces interact via the adatoms when separated, as seen in Fig. 5. These adatoms would tend to have greater fluctuations in the z direction interacting with each other than if they were interacting with a static cleaving potential. They should therefore be more likely to move onto other adatoms sites or displace atoms underneath them, which should result in better statistics. The work obtained from the system in this expansion is roughly 5% of the work put into the system in the first part. For comparison, ab initio calculation results at T=0 K performed by L.Vitos et al. adopting the FCD method[27] is shown in Fig. 3.

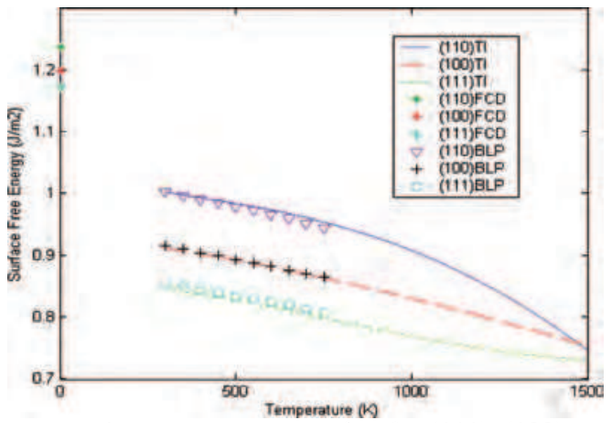

Fig. 3. Solid surface free energies vs temperature for the (111), (100), and (110) faces obtained using the thermodynamic integration technique and the lambda integration method. Also shown are L. Vitos et al.'s FCD results at 0 K. (Picture redrawn from Ref. 17)

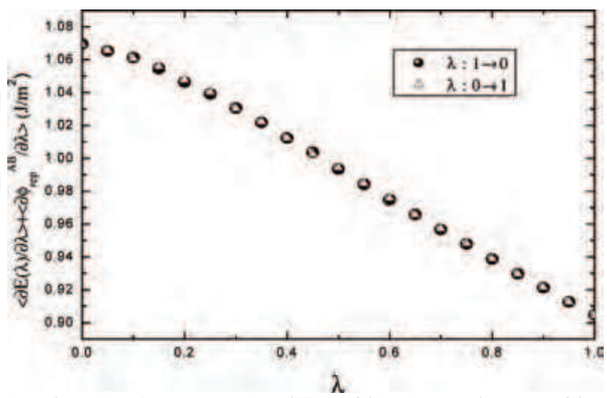

Fig. 4. Simulation results for the integrand $<\partial E(\lambda)/\partial\lambda>\lambda + <\partial\varphi_{rep}^{AB}/\partial\lambda>\lambda$ for the (110) face at 750 K. (Picture redrawn from Ref. 17)

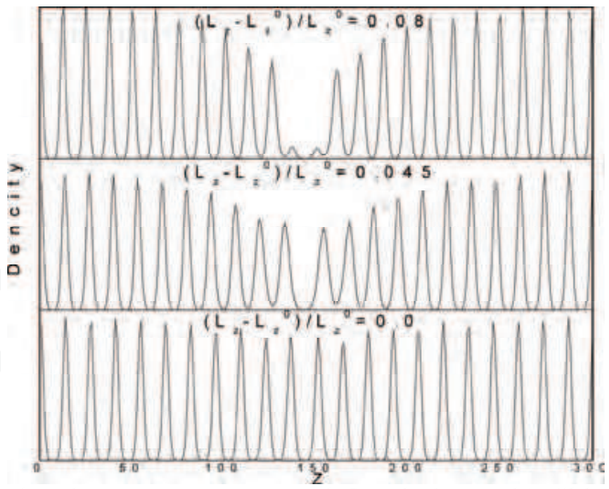

Fig. 5. z density plots for the expansion part of Grochola et al.'s "blanket lambda" path at $(L_z - L_z^0)/\ L_z^0$ = 0, 0.045, and 0.08 applied to the (110) face at a temperature of 750 K. (Picture redrawn from Ref. 17)

The calculated average solid surface free energy is shown in Fig. 6. Also shown are the liquid surface free energies and their linear fitting values, $\gamma_L(T) = 0.5773 - 2.3051 \times 10^{-4}(T - 1243)$. At melting point, we acquire the solid surface free energy and the liquid surface free-energy values of 0.793 J/m^2 and 0.577 J/m^2, respectively. The semi-theoretical estimates of Tyson and Miller[28] for the solid surface energy at T_{mb} are 1.086 (J/m^2), and the experimental value[29] for the surface energy of the solid and the liquid states at T_{mb} are 1.205 and 0.903 (J/m^2), respectively. It should be emphasized that surface free energies of crystalline metals are notoriously difficult to measure and the spread in experimental values for well-defined low-index orientations is substantial, as Bonzel et al.[30] pointed out.

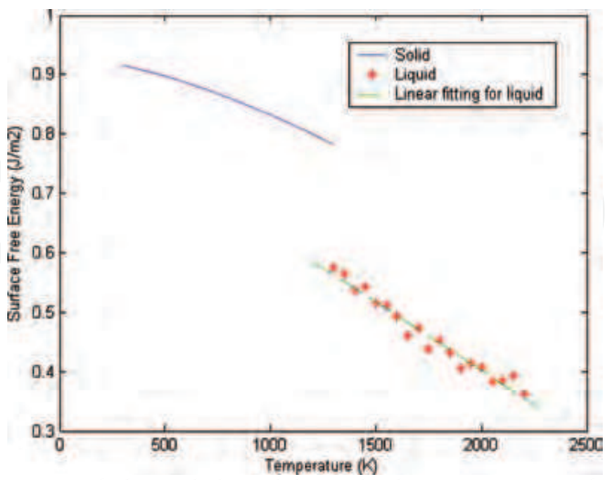

Fig. 6. Surface free energy of the solid and liquid phase in units of J/m^2 as a function of temperature. The data for liquid surface free energy is fitted to a linear function of temperature. (Picture redrawn from Ref. 17)

It is obvious that because MAEAM is developed using only bulk experimental data, it underestimates surface free energy in both the solid and the liquid states as many EAM models do.[31,32] Though there is the difference between the present results and experimental estimates, we note that the surface free-energy difference between the solid and liquid phase is 0.216 (J/m^2) and is between Tyson and Miller's result of 0.183 (J/m^2) and the experimental value of 0.3 (J/m^2). Furthermore, the average temperature coefficient of the solid and liquid phase surface free energy is 1.32×10^{-4} (J/m^2K) and 2.3×10^{-4} (J/m^2K), respectively. Such values compare reasonably well with Tyson and Miller's estimate of 1.3×10^{-4} (J/m^2K)[28] for the solid and the experimental results of 1.6×10^{-4} (J/m^2K)[33] for the liquid. Therefore, we expect the model to be able to predict the melting points of nanoparticles by means of determining the intersection of free-energy curves. Because the liquid surface free energy is lower than the solid surface free energy, the solid and liquid free-energy curves of nanoparticles change differently when the size of the nanoparticle decreases so that the melting points of nanoparticles decrease with decreasing particle size, as is depicted by Fig. 7. This indicates actually that the surface free-energy difference between the solid and liquid phase is a decisive factor for the size-dependent melting of nanostructural materials.

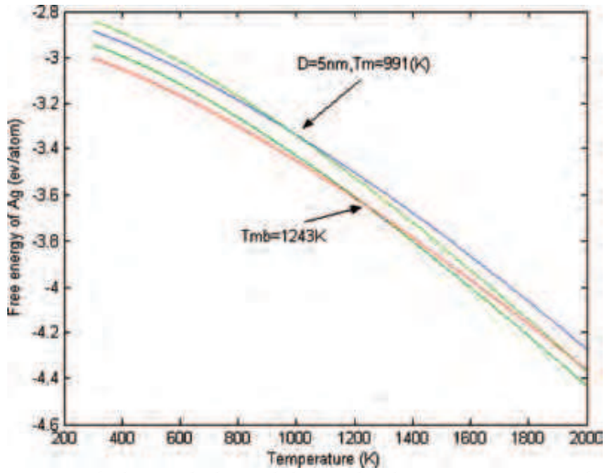

Fig. 7. Gibbs free energies of the solid and liquid phase in units of eV/atom for the bulk material and 5 nm nanoparticle. (Picture redrawn from Ref. 17)

In order to test our model, we plotted the results for the melting temperature versus inverse of the particle diameter in Fig. 8. Because there is no experimental data available for the melting of Ag nanoparticles, the predictions of Nanda et al.[10] and Yang et al.'s[34] theoretical model are shown in Fig. 8 for comparison. It can be seen that agreement between our model and Nanda et al.'s[10] theoretical predictions for Ag nanoparticles is excellent. The nonlinear character of the calculated melting curve results from the temperature dependence of the surface free-energy difference between the solid and liquid phase, which is neglected in Nanda et al.'s[10] model. Alternatively, Yang et al.'s[34] theoretical predictions may overestimate the melting point depression of Ag nanoparticles.

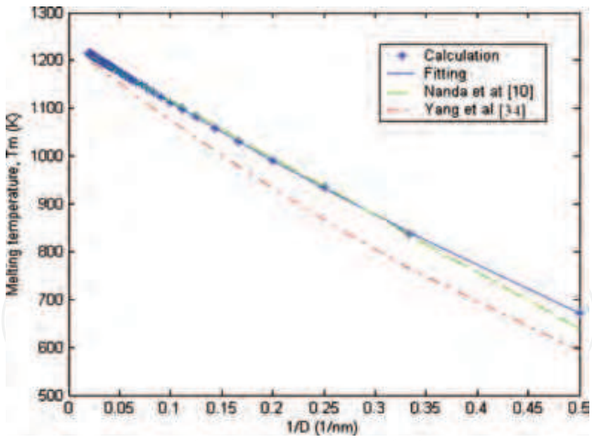

Fig. 8. Melting point vs the reciprocal of nanopartical diameter. The solid line is the fitting result. The dashed line is the result calculated from the thermodynamic model $T_m = T_{mb}(1 - \beta/d)$,[10] ($\beta$ = 0.96564). (Picture redrawn from Ref. 17)

It is believed that understanding and predicting the melting temperature of nanocrystals is important. This is not only because their thermal stability against melting is increasingly becoming one of the major concerns in the upcoming technologies[1,34,35] but also because many physical and chemical properties of nanocrystals follow the exact same dependence on the particle sizes as the melting temperature of nanocrystals does. For example, the size-dependent volume thermal expansion coefficient, the Debye temperature, the diffusion activation energy, the vacancy formation energy, and the critical ferromagnetic, ferroelectric, and superconductive transition temperature of nanocrystals can be modeled in a fashion similar to the size-dependent melting temperature.[34,36,37] However, Lai et al.[38] pointed out that in order to understand the thermodynamics of nanosized systems comprehensively an accurate experimental investigation of "the details of heat exchange during the melting process, in particular the latent heat of fusion" is required. Allen and co-workers developed a suitable experimental technique to study the calorimetry of the melting process in nanoparticles and found that both the melting temperature and the latent heat of fusion depend on the particle size.[38-40] Here we calculate the molar heat of fusion and molar entropy of fusion for Ag nanoparticles, and the results are shown in Fig. 9. It can be seen that both the molar heat and entropy of fusion undergo a nonlinear decrease as the particle diameter D decreases. In analogy with the melting point, Figure 9 shows that the system of smallest size possesses the lowest latent heat of fusion and entropy of fusion. In a particle with a diameter of 2.5 nm or smaller, all of the atoms should indeed suffer surface effects, and the latent heat of fusion and the entropy of fusion are correspondingly expected to vanish. It is also observed that the size effect on the thermodynamic properties of Ag nanoparticles is not really significant until the particle is less than about 20 nm.

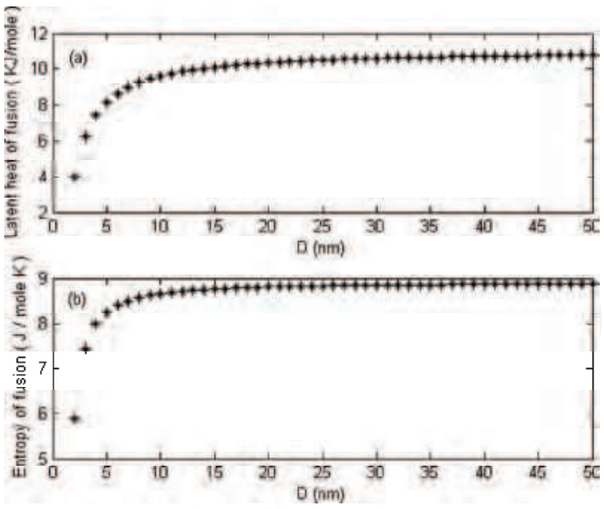

Fig. 9. (a) Molar latent heats of fusion ΔH_m and (b) molar entropy of fusion ΔS_m of Ag nanoparticals as a function of particle diameter D. (Picture redrawn from Ref. 17)

Figure 10 plots the molar heat capacities as a function of temperature for bulk material and nanoparticles. One can see that the molar heat capacity of nanoparticles increases with increasing temperature, as the bulk sample does. The temperature dependence of molar heat capacity qualitatively coincides with that observed experimentally. Figures 10 and 11 show that the molar heat capacity of bulk sample is lower compared to the molar heat capacity of the nanoparticles, and this difference increases with the decrease of particle size. The discrepancy in heat capacities of the nanoparticles and bulk samples is explained in terms of the surface free energy. The molar heat capacity of a nanoparticle consists of the contribution from the bulk and surface region, and the reduced heat capacity C/C_b (C_b denotes bulk heat capacity) varies inversely with the particle diameter D. Likhachev et al.[41] point out that the major contribution to the heat capacity above ambient temperature is determined by the vibrational degrees of freedom, and it is the peculiarities of surface phonon spectra of nanoparticles that are responsible for the anomalous behavior of heat capacity. This is in accordance with our calculation. Recently, Li and Huang[42] calculated the heat capacity of an Fe nanoparticle with a diameter around 2 nm by using MD simulation and obtained a value of 28J/mol·K, which is higher than the value of 25.1J/mol·K[22] for the bulk solid. It might be a beneficial reference data for understanding the surface effect on the heat capacity of nanoparticles. The ratio C/C_b=1.1 they obtained for 2 nm Fe nanoparticles is comparative to our value of 1.08 for 2 nm Ag nanoparticles. Because we set up a spherical face by three special low-index surfaces, the molar heat capacity of nanoparticles necessarily depends on the shape of the particle.

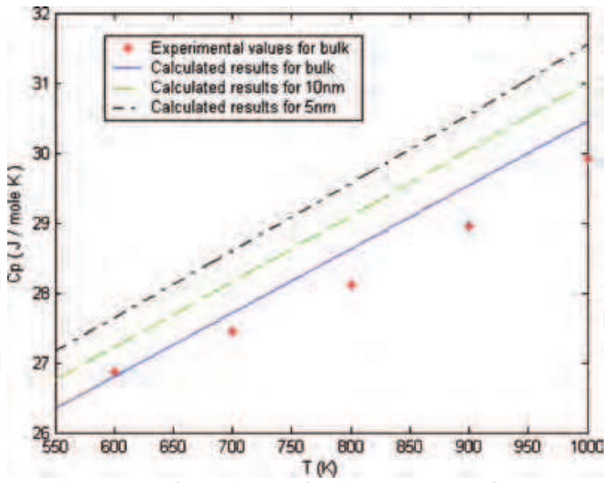

Fig. 10. Molar heat capacity as a function of temperature for Ag nanoparticles and bulk sample. (Picture redrawn from Ref. 17)

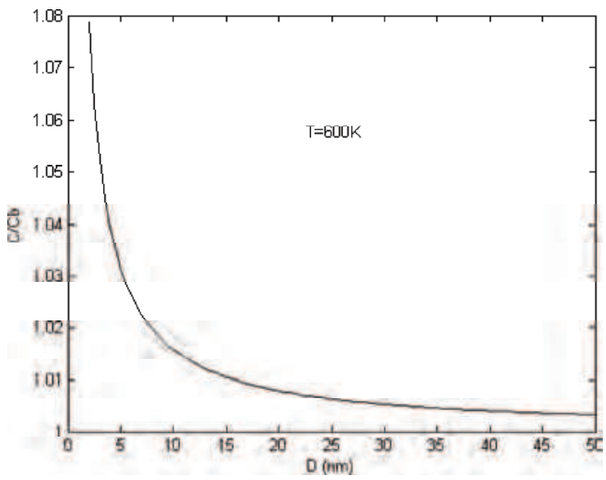

Fig. 11. Dependence of heat capacities of Ag nanoparticles with different sizes relative to the bulk sample. C_b is the heat capacity of the bulk sample. (Picture redrawn from Ref. 17)

The molar entropy as a function of temperature is shown in Fig. 12. It can be seen that the calculated molar entropies are in good agreement with experimental values.[22] The molar entropy of nanoparticles is higher than that of the bulk sample, and this difference increases with the decrease of the particle size and increasing temperature. According to Eq. 7, the reduced molar entropy S/S_b (S_b denotes bulk entropy) also varies inversely with the particle diameter D, just as the heat capacity of a nanoparticle does. Because entropy is only related to the first derivatives of Gibbs free energy with regard to temperature, and we have obtained the average temperature coefficient of solid surface energy agreeing with the value in literature,[28] it may be believed that Fig. 12 rightly reveals the molar entropy of nanoparticles.

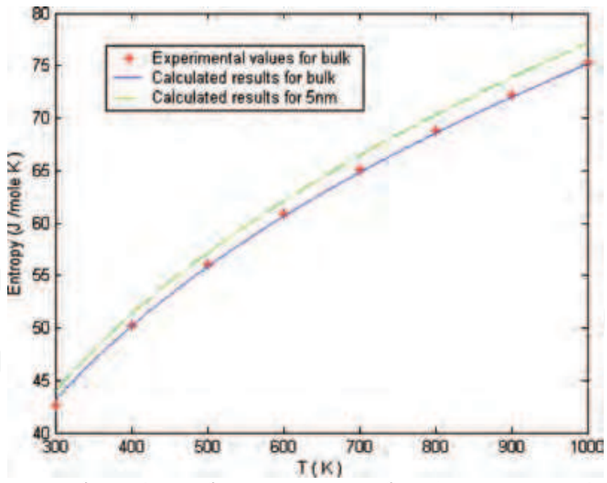

Fig. 12. Molar entropy as a function of temperature for Ag nanoparticles and bulk material. (Picture redrawn from Ref. 17)

2. Grain growth of nanocrystalline silver

Nanocrystalline materials are polycrystalline materials with mean grain size ranging from 1 to 100 nm. Affected by its unique structural characteristics, nano-sized grains and high fraction of grain boundary, nanocrystalline materials possess a series of outstanding physical and chemical properties, especially outstanding mechanical properties, such as increased strength/hardness and superplastic [43]. However, just because of the high ratio of grain boundary, the nanocrystalline materials usually show low structural stability, the grain growth behavior directly challenges the processing and application of nanocrystalline materials. How to improve the thermal stability of nanocrystalline materials became a challenging study.

Since the network of grain boundary (GB) in a polycrystalline material is a source of excess energy relative to the single-crystalline state, there is a thermodynamic driving force for reduction of the total GB area or, equivalently, for an increase in the average grain size [44]. Especially as grain size decreases to several nanometers, a significant fraction of high excess energy, disordered GB regions in the nanostructured materials provide a strong driving force for grain growth according to the classic growth theory [45]. In contrast to the microcrystal, recent theoretical and simulation studies indicate that grain boundary motion is coupled to the translation and rotation of the adjacent grains [46]. How Bernstein found that the geometry of the system can strongly modify this coupling [47]. We simulate the grain growth in the fully 3D nanocrystalline Ag. It is found that during the process of grain growth in the nanocrystalline materials, there simultaneously exist GB migrations and grain rotation movements [46,48,49]. The grain growth of nanocrystalline Ag exhibits a Power law growth, followed by a linear relaxation process, and interestingly the dislocations (or stacking faults) play an important intermediary role in the grain growth of nanocrystalline Ag.

For conventional polycrystalline materials, the mechanism of grain growth is GB curvature-driven migration [44]. Recently, the grain rotation mechanism has been found both in the experiments and simulations [46,48,49]. These two mechanisms are also found in our

simulations as illustrated in Fig. 13 and Fig. 14, respectively. Fig. 13 shows the GB migration in a section perpendicular to Z-axis in the course of grain growth for the 6.06 nm sample at 1000 K. It is clear that the grain 1, as a core, expands through GB migrating outwards until the whole nanocrystal closes to a perfect crystal. Fig. 14 shows the atomic vector movement in the same section as in Fig.13 from 200ps to 320ps, the grain 1 and grain 2 reveal obvious rotation, although these two grains don't coalesce fully by their rotations.

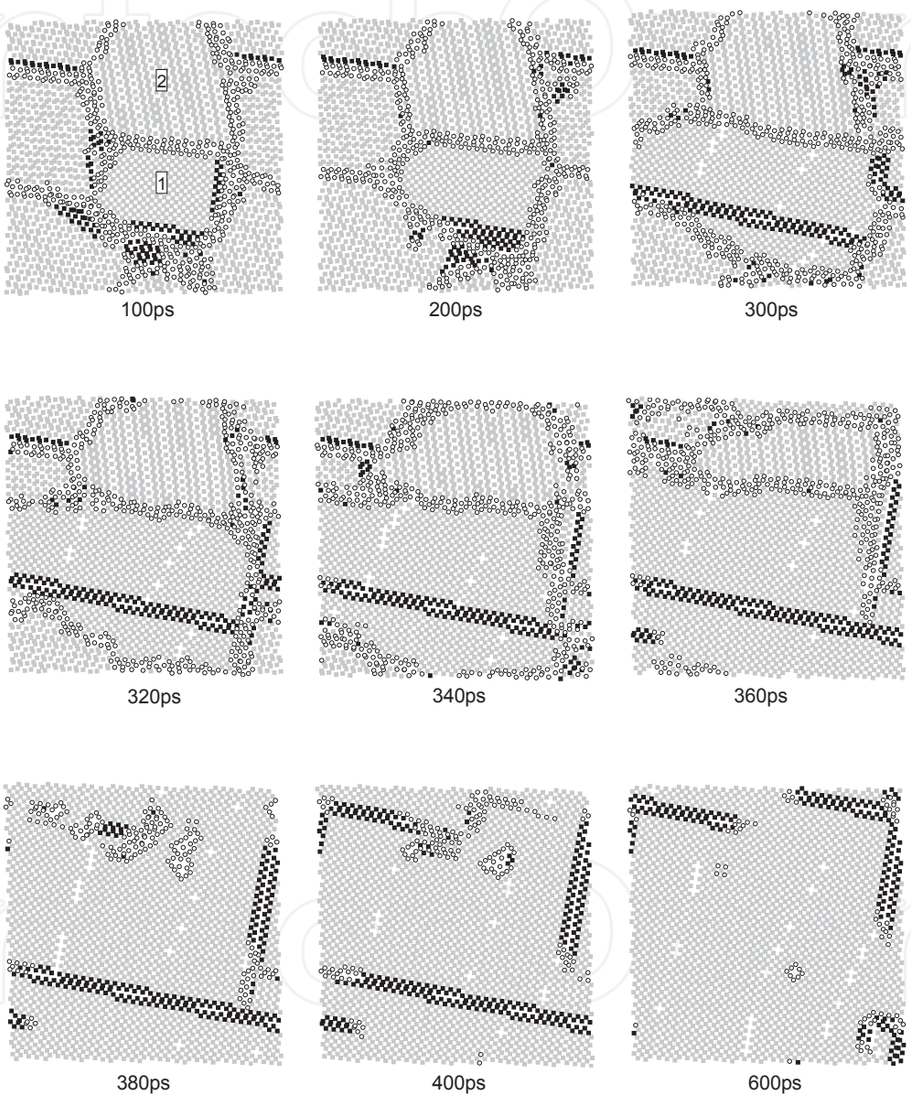

Fig. 13. The typical structural evolution of a section perpendicular to Z-axis during grain growth by GB migration for the 6.06nm specimen at 1000K, the grey squares represent FCC atoms, the black squares for HCP atoms and the circles for the other type atoms, respectively. (Picture redrawn from Ref. 48)

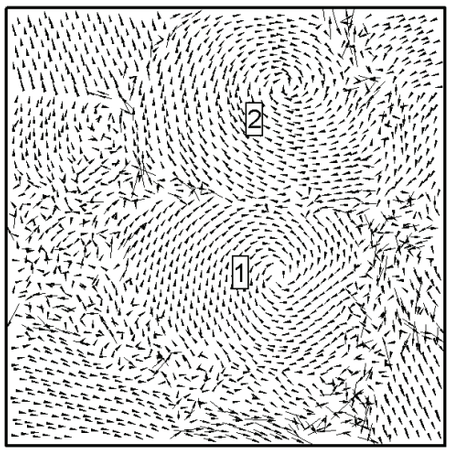

Fig. 14. Atomic vector movement in the same section as in Fig.3 from 200ps to 320ps, the grains 1 and 2 exhibit obvious rotations. (Picture redrawn from Ref. 48)

Figure 15 shows the quantitative evolution of FCC atoms for the 6.06 nm sample at 900 K and 1000 K, respectively. Affected by thermally activated defective atoms at the beginning of imposing thermostat, the number of atoms with FCC structure decreases with the relaxation time (as triangle symbols shown in Fig. 15). Subsequently the grains begin to grow up. It is evident that the process of grain growth can be described as a Power law growth, followed by a linear relaxation stage. In the Power law growth stage, the growth curves are fitted as follows:

$$C = C_0 + Kt^n \tag{11}$$

where C is the proportion of FCC atoms, K is a coefficient and n is termed the grain growth exponent, and the fitted values of n are 3.58 and 3.19 respectively for annealing temperature 1000 K and 900 K. The values of n, which indicate their growth speeds, increase with increasing the annealing temperature. In the Power law growth stage, the grain growth is mainly dominated by the GB migration. In the succedent linear relaxation process, the fraction of FCC atoms increases linearly with time, and this increment mostly comes from the conversion of the fault clusters and dislocations (or stacking faults) left by GB migration (as shown in Fig. 13). In addition, it is noted that the change from Power law growth to linear relaxation is overly abrupt, this is because the sampled points in the structural analysis are very limited and there exists a bit of fluctuation in the structural evolution.

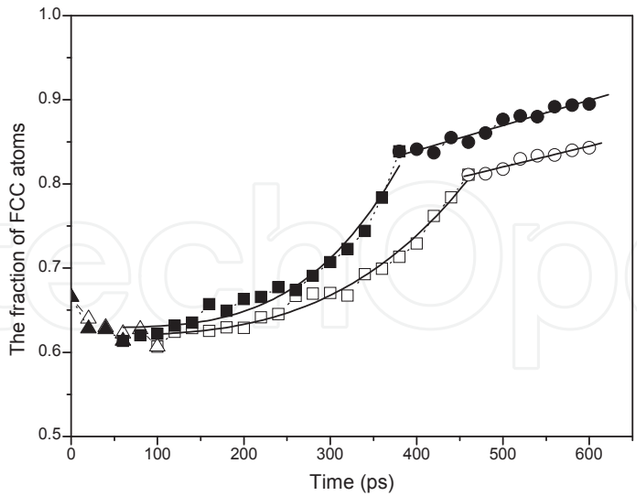

Fig. 15. The isothermal evolution of the fraction of FCC atoms with time for the 6.06nm sample, the solid and the open symbols represent the fraction at 1000K and at 900K, respectively. The triangles represent the thermally disordered stage, the squares for the Power law growth stage, and the circles for the linear relaxation process. (Picture redrawn from Ref. 48)

Besides GB migration and grain rotation, the dislocations (or stacking faults) may play an important role in grain growth of FCC nanocrystals. From the structural analysis it is found that along with the grain growth, the fraction of HCP atoms undergoes a transformation from increasing to decreasing. Comparing the evolution of FCC and HCP atoms with time, the critical transformation time from HCP atoms increasing to decreasing with annealing time is in accordance with the turning point from the Power law growth stage to the linear relaxation stage. At the Power law growth stage, dislocations (or stacking default) are induced after the migration of GB (as shown in Fig. 13), and the fraction of HCP atoms increases. Their configuration evolves from the dispersive atoms and their clusters on GB to aggregative dislocations (or stacking faults) as shown in Fig. 16. Turning into the linear relaxation stage, the fraction of HCP atoms decreases with the annealing time gradually, and some dislocations (or stacking defaults) disappear (as shown in Fig. 13 and Fig. 16). Comparing with the interface energy (about 587.1 mJ/m^2 and 471.5 mJ/m^2 for the 6.06 nm and 3.03 nm samples, respectively, if supposing grains as spheres and neglecting the triple-junction as well as high-junction GBs), although stacking default energy is very small for Ag (14.1 mJ/m^2), the evolutive characteristic of HCP atoms during grain growth is probably correlative with the stacking fault energy, which lowers the activation energy for atoms on GB converting into stacking faults than directly into a portion of grains, so the dislocations (or stacking faults) may act as the intermediary for the atom transforming from GB to grains.

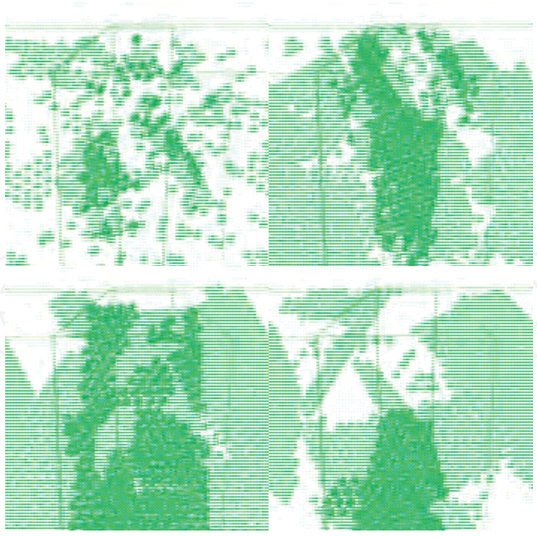

Fig. 16. HCP atoms configuration evolution during grain growth process for the 6.06nm specimen at 1000K. (Picture redrawn from Ref. 48)

3. Melting behaviour of Nanocrystalline silver

Melting temperature (T_m) is a basic physical parameter, which has a significant impact on thermodynamic properties. The modern systematic studies have provided a relatively clear understanding of melting behaviors, such as surface premelting [50,51], defect-nucleated microscopic melting mechanisms [52], and the size-dependent T_m of the low dimension materials [10]. In recent years, the unusual melting behaviors of nanostructures have attracted much attention. On a nanometer scale, as a result of elevated surface-to-volume ratio, usually the melting temperatures of metallic particles with a free surface decrease with decreasing their particle sizes [7,35], and their melting process can be described as two stages, firstly the stepwise premelting on the surface layer with a thickness of 2-3 perfect lattice constant, and then the abrupt overall melting of the whole cluster.[53] For the embedded nanoparticles, their melting temperatures may be lower or higher than their corresponding bulk melting temperatures for different matrices and the epitaxy between the nanoparticles and the embedding matrices [54]. Nanocrystalline (NC) materials, as an aggregation of nano-grains, have a structural characteristic of a very high proportion of grain boundaries (GBs) in contrast to their corresponding conventional microcrystals. As the mean grain size decreases to several nanometers, the atoms in GBs even exceed those in grains, thus, the NC materials can be regarded as composites composed by grains and GBs with a high excess energy. If further decreasing the grain size to an infinitesimal value, at this time, the grain and GB is possibly indistinguishable. What about its structural feature and melting behavior? We have reported on the investigation of the melting behavior for "model" NC Ag at a limited grain-size and amorphous state by means of MD simulation, and give an analysis of thermodynamic and structural difference between GB and amorphous state.[55,56]

Figure 17 shows the variation of T_m of NC Ag and the solid-to-liquid transformation temperature of amorphous state Ag. It can be seen that, from grain-size-varying nanocrystal

to the amorphous, the curve of T_m exhibits three characteristic regions named I, II and III as illustrated in Fig. 17. In addition, considering the nanocrystal being an aggregation of nanoparticles, the T_m of nanoparticles with FCC crystalline structure is appended in Fig. 17.

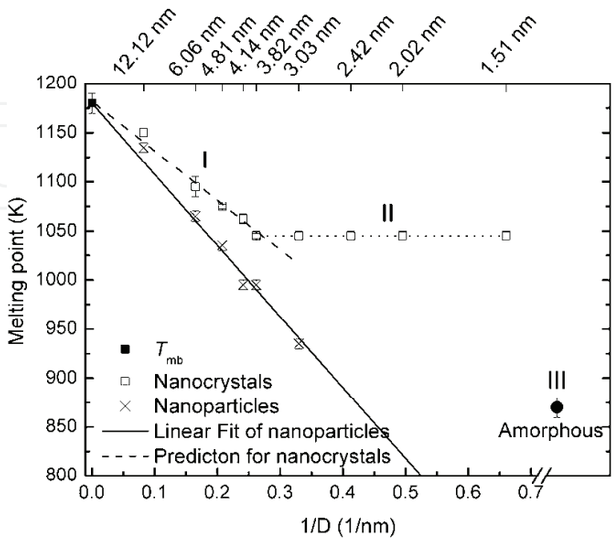

Fig. 17. Melting temperature as a function of the mean grain size for nanocrystalline Ag and of the particle size for the isolated spherical Ag nanoparticles with FCC structure, and the solid-to-liquid transformation temperature of amorphous state. (Picture redrawn from Ref. 56)

In region I, in comparison to T_m (bulk) = 1180±10 K simulated from the solid-liquid coexistence method with same modified analytical embedded atom method (MAEAM) potential, the melting temperatures of the NC Ag are slightly below T_m (bulk) and decrease with the reduction of the mean grain size. This behavior can be interpreted as the effects of GBs on T_m of a polycrystal. MD simulations on a bicrystal model have shown that an interfacial melting transition occurs at a temperature distinctly lower than T_m (bulk) and the width of interfacial region behaving like a melt grows significantly with temperature [57]. This will induce the grains in a polycrystal melted at a temperature lower than T_m (bulk) when the mean grain size decreases to some extent and results in the depression of T_m for the NC materials.

Comparing with the corresponding nanoparticle with the same size, the NC material has a higher T_m. This is to be expected since the atoms on GB are of larger coordination number than those on a free surface, and the interfacial energy (γ_{GB}) is less than the surface energy (γ_{Sur}). It is well known that the main difference between the free particles and the embedded particles or grains in a polycrystal is the interfacial atomic structure. A thermodynamic prediction of T_m from a liquid-drop model [10] for free particles was proposed as follows

$$T_m = T_{mb}(1-(\beta / d)) \tag{12}$$

where T_{mb} is the melting temperature for conventional crystal, β is a parameter relative to

materials, d is the mean diameter of the grain. Through the linear fitting of the data from the MD simulations in terms of Eq.(12), the value of β for Ag nanoparticles is determined as 0.614, which is lower than that from thermodynamic prediction, and this tendency is the same for several other elements [58]. Considering the difference between the interfacial energy and the surface energy, an expression describing the mean grain size-dependent T_m for the NC materials is proposed as follows:

$$T_m = T_{mb}(1-(\beta / d)(1-\gamma_{GB} / \gamma_{Sur})) \quad (13)$$

where γ_{GB} =375.0 mJ/m^2 [59] and γ_{Sur} =1240.0 mJ/m^2 [28] for Ag. Based on the fitted value β=0.614, the prediction of T_m of the NC Ag from Eq.(13) gives a good agreement with the values from the MD simulations as shown in Fig. 17. Thus, the melting temperatures of the NC materials can be qualitatively estimated from the melting temperatures of the corresponding nanoparticles.

Contrasting Eq.(13) with Eq.(12), the difference of T_m of nanocrystal from that of corresponding size spherical nanoparticle is induced by the distinction of properties between grain boundary and free surface. This further indicates the grain size dominated T_m of nanocrystalline Ag in region I.

Whereas in region II, the value of T_m almost keeps a constant, that is to say, the T_m of nanocrystalline Ag in this size region is independent on grain size. This tendency of T_m for nanocrystals is not difficult to understand from its remarkable size-dependent structure. According to the structural characteristic of small size grains and high ratio of grain boundary network, the nanocrystal can be viewed as a composite of a grain boundary phase and an embedded grain phase. As mean grain size is large enough, the grain phase is the dominant one, and the T_m of nanocrystals is correlated with their grain size. With mean grain size decreasing to a certain degree, the grain boundary phase becomes dominant, and the T_m of nanocrystal is possibly dominated by grain boundary phase. So the melting temperature of limited nanocrystalline materials can be considered as the T_m of grain boundary phase. Actually, these similar size-dependent physical properties of nanocrystals have been found recently in the mechanical strength of nanocrystalline Cu.[60] In region III (i.e. from nanocrystal to amorphous state), there exists a sharp decrease in T_m. This remarkable difference in T_m is a manifestation of fundamental difference in structure between nanocrystal/GB and amorphous state.

To further the investigation of size effect on the T_m of nanocrystal, the local atomic structure is analyzed with CNA. According to the local atomic configurations from the CNA, the atoms are classified into three classes: FCC, HCP and the others. Comparing the structural characteristic before and after annealing process (as shown in Fig. 18), the difference increases with decreasing the grain size because of the enhanced GB relaxation and instability in smaller size samples. Especially for the sample with a grain size of 1.51 nm, it shows minor grain growth. For nanocrystalline Ag, as the mean grain size below about 4 nm, the fraction of GB exceeds that of grain. This size exactly corresponds to the critical transformation size from the size-dependent T_m region to size-independent one. Within the small grain-size range, although the fraction of GB and mean atomic configurational energy keep on increasing with grain size decreasing, the T_m of nanocrystal is almost invariable, which provides the evidence of GB dominated T_m in this size range.

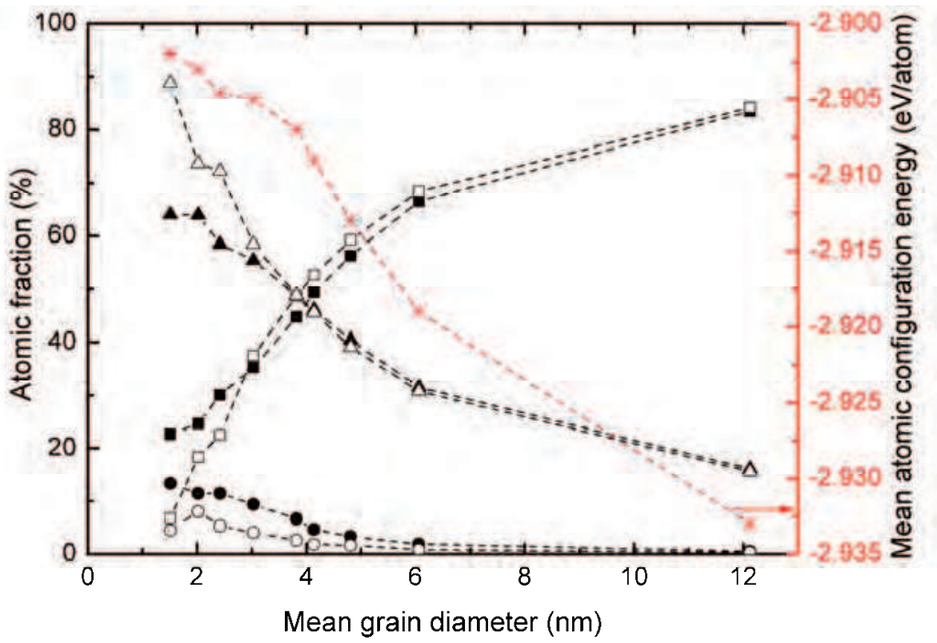

Fig. 18. The grain size-dependent structure and mean atomic configuration energy (Stars) of nanocrystalline Ag. The Squares, Circles and Triangles represent the atoms with local FCC, HCP and other type structure, and the open symbols and solid ones denote the case before and after annealing process, respectively. (Picture redrawn from Ref. 56)

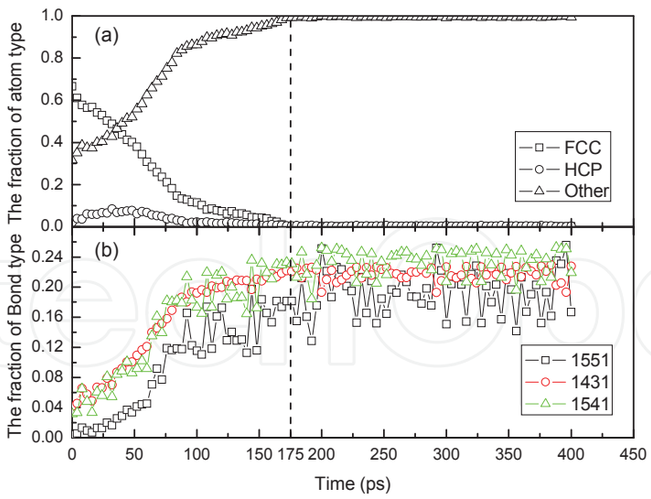

Fig. 19. The typical bond-type existing in the liquid phase and atom-type (from CNA analysis) evolution with MD relaxation time for specimen with a mean grain size of 6.06 nm (T_m: 1095±5K) at 1100K. (Picture redrawn from Ref. 57)

According to the local atomic configurations from the CNA, we observed the evolution of

grains and GBs during the melting process. Figure 19 shows the relative number of three structural classes of atoms (a) and that of typical bonded pairs existing in metallic liquid (b) as a function of heating time during melting. With the melting developing, the fraction of atoms with a local FCC structure drops rapidly from an initial value of 66.6% to 0 at 175ps, as the NC material turns into a liquid phase completely. On the contrary, the relative numbers of the three typical bonded-pairs (1551), (1431) and (1541), which indicates the liquid (or like liquid) structural characteristics, increase rapidly from 0.4%, 4.1% and 3.2% to the average values of 19.2%, 21.7% and 23.3%, respectively, i.e. the fraction of the liquid phase (or like liquid) increases. It reveals that the melting in the polycrystals is a gradual process with heating time. Corresponding to a quantitative description on structural evolution (shown in Fig. 19), Figure 20 illustrates the 3-dimentional snapshots of grains in the NC material during melting. It is found that the melting in the polycrystals stars from GB. Along with melting, the interfacial regions (liquid or like liquid) between grains widen and the grains diminish till absolutely vanish.

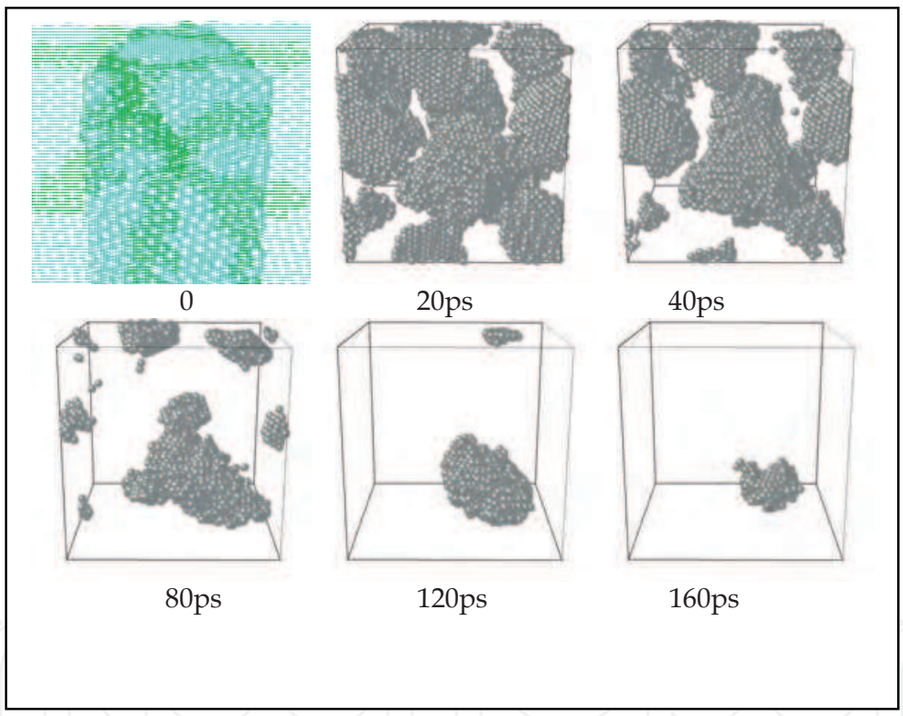

Fig. 20. Three-dimensional snapshots of atomic positions in the course of melting for specimen with a mean grain size of 6.06 nm at 1100K, the grey spheres denote atoms with a local FCC structure and the black spheres denote the other type of atoms on GB. For clarity, only FCC atoms are sketched during melting. (Picture redrawn from Ref. 57)

As well known, the crystallization from amorphous materials is an effective technique in the fabrication of nanocrystals.[61] On the contrary, it is found that the so-called nanocrystal, with the grain size extrapolating to an infinitesimal value during the Voronoi construction, has a similar structure as that of the amorphous from rapid quenching of liquid. They have similar RDF with the characteristic of the splitting of the second peak for an amorphous state. The relative numbers of the three typical bond pairs (1551), (1431) and (1541) in two

amorphous samples from different processes (as listed in TABLE 1), are very close respectively. The slight difference on the percentage of corresponding type of bond pair is because the annealing temperature and quenching speed have a little influence on the amorphous structure. In addition, the two amorphous samples have the same solid-to-liquid temperature of 870±10 K. In other words, the Voronoi construction is an effective method in the construction of amorphous model.

Size (nm)	1551 (%)	1431 (%)	1541 (%)
Amorphous [a]	10.26	20.49	21.02
Amorphous [b]	14.56	21.47	23.73
1.51	2.25	16.75	18.69
2.02	2.51	17.38	20.23
2.42	2.03	16.65	18.24
3.03	1.78	15.75	15.85
3.82	1.78	15.27	14.26
4.14	2.05	15.49	14.03
4.81	1.90	15.18	13.56
6.06	1.39	13.14	10.01
12.12	1.36	12.73	9.83

[a] The amorphous is obtained from the rapid quenching of liquid.
[b] The amorphous is obtained from the annealing of the Voronoi construction.
Table 1. Fraction of three typical bond pairs (1551), (1431) and (1541) existing in non-crystalline structure from common neighbor analysis.

On the structural difference between GB and amorphous state, there is a long standing argument. Presently, the prevalent viewpoint is that the structure of GB is different from that of amorphous state[62,63], but the intrinsic difference is still not fully understood yet. Here if excluding the grain phase in nanocrystal, from TABLE 1, one can see the fraction of bond pairs (1431) and (1541) shows approximately consecutive increase with decreasing the mean grain size of nanocrystal gradually to an amorphous state, which indicates the increase of disordered degree in GB. Whereas the fraction of bond (1551) indicating fivefold symmetry have no evident change with grain size in nanocrystal. Once turning into amorphous state, there is a sharp increase in the proportion of bond pair (1551). So we concluded that the main difference between grain boundary and amorphous state lies in the higher fivefold symmetry in the latter.

4. Solidification of liquid silver and silver nano-drop

The crystallization from liquid is one of the important issues in crystal-growth technology. Just from the transformation of state of matter, crystallization from liquid is a reverse process of the melting, but there is much difference in thermodynamics and kinetics of phase transition between them. For instance, the spontaneous crystallization can only occur via homogeneous nucleation, a thermally activated process involving the formation of a growing solid nucleus. That is why the supercooling phenomenon is more ubiquitous than

the superheating one experimentally.[64] So far, with the molecular dynamics simulation, a lot of work about crystallization has been made on the size of critical nucleus,[65,66] the structural feature of nucleus,[67,68] and the effect of cooling rate on the crystalline texture.[69] Beside the widely studied metallic materials, recently there is some work on the crystallization process of covalent and molecular crystals.[70-72] Here we mainly focus on the isothermal structural evolution in the course of crystallization. By means of tracking the evolution of local atomic structure, the processes of crystallization at a certain temperature are well observed.

As mentioned above, the melting temperature of conventional Ag from simulation is 1180 K. However, once the sample turned into liquid completely, it didn't crystallize till temperature cooling down to 850 K. This is because the homogeneous nucleation from liquid needs a certain driving force, which is closely correlated with supercooling temperature according to the classic theory of nucleation. Here we have considered three supercooling degree (from 850K to 800K, 750K and 700K respectively) to investigate its effect on crystallization process. The temperature-dependent mean atomic energy is shown in Fig. 21. One can find that there occurs abrupt drop of energy at the temperature of 800 K, 750 K, and 700 K against that at liquid state, which is a signature of phase transition taking place at these temperature points. This also has been confirmed by the structural transformation from the analysis of CNA.

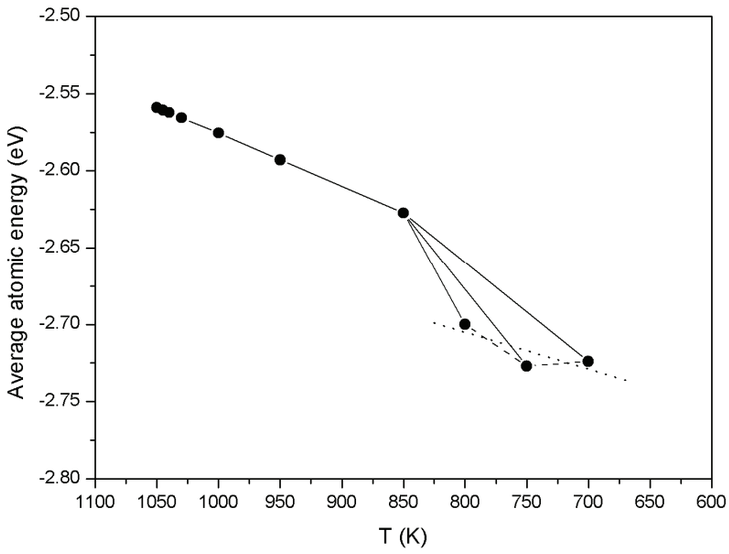

Fig. 21. The temperature-dependent mean atomic energy curves during cooling process. (Picture redrawn from Ref. 74)

Figure 22 shows the mean atomic configurational energy and mean atomic volume as a function of time during crystallization at 800 K, 750 K and 700 K. The energy and volume have similar changing trend for they each are correlative with the arrangement of atoms. From the evolution of energy and volume, the curves can be separated into three characteristic regions, which correspond to the three physical stages of the isothermal crystallization from liquid: nucleation, rapid growth of nuclei and slow structural relaxation. Contrasting the three curves at indicated temperatures, as temperature decreases, i.e. the

enhancement of supercooling degree, the consumed time in the process of nucleation reduces obviously. This is because, according to the classic theory of nucleation, the critical size of nuclei decreases and the nucleation rate increases with supercooling degree increasing. As temperature decreasing to 700 K, the transition from nucleation to rapid growth of nuclei becomes ambiguous. Interestingly, after a relatively long period of slow structural relaxation, the mean atomic configurational energy at 700 K even is larger than that at 800 K. This is because the high rate of nucleation generally results in a large number of grains in unit volume, and thus a high proportion of grain boundary network. In addition, the much higher supercooling degree inhibits the atomic motion, and the defects within the grains increase. This high supercooling-degree technique has a potential application in the fabrication of nanocrystals by crystallization from liquid.

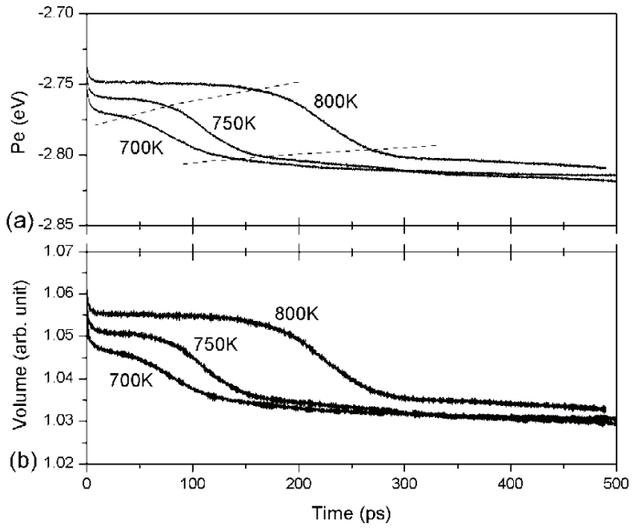

Fig. 22. The mean atomic configuration energy (a) and mean atomic volume (b) as a function of time during crystallization at 800 K. (Picture redrawn from Ref. 74)

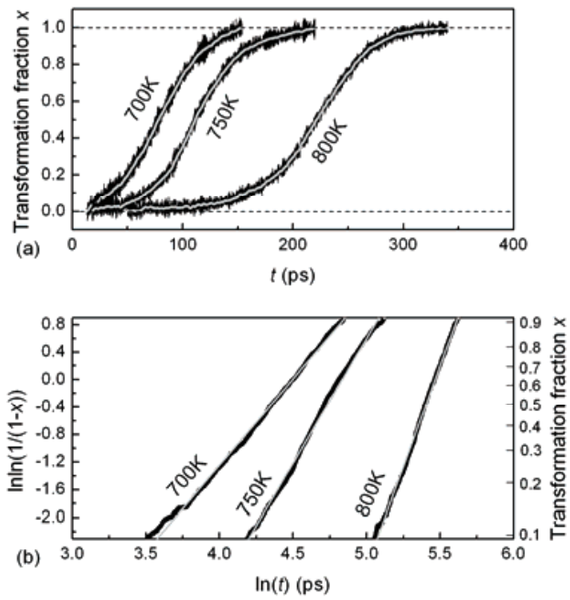

Fig. 23. The variation of volume transformation fraction of solid with time at indicated temperatures. (Picture redrawn from Ref. 74)

Supposing the systematic volume of a liquid-solid mixture is a linear superposition of its constituents, the volume transformation fraction can be determined from the following expressions:

$$V(t) = (1 - x(t))\, V_l + x(t)\, V_s \tag{14}$$

where V_l and V_s are the volume of unit liquid and solid at a certain temperature respectively, and $V(t)$ and $x(t)$ represent the variation of systematic volume and volume fraction of solid with time respectively. The values of V_l and V_s can be defined from the systematic volume before nucleation and after the completion of rapid growth of nucleus respectively. Based on the volume evolution in the stages of nucleation and rapid growth of nucleus as in Fig. 22(b), the typical "S" curves of transformation fraction of solid from liquid are shown in Fig. 23(a). For kinetic analysis of phase transition from liquid to solid, the Johnson-Mehl-Avrami (JMA) equation was used: [73,74]

$$x(t) = 1 - \exp(-K_T t^n) \tag{15}$$

where K_T is the constant of reaction rate and n is the Avrami exponent. The rate constant and the Avrami exponent are obtained from a plot of ln(-ln((1-x(t))) vs. ln(t) as shown in Fig. 23(b) and the fitted parameters are listed in Table 2.

T (K)	n	K_T
800	5.84	1.33×10^{-14}
750	3.62	2.46×10^{-8}
700	2.50	1.29×10^{-5}

Table 2. The fitted kinetic parameters at different temperatures of crystallization by JMA equation.

The Avrami exponent decreases with increasing supercooling degree, which indicates the supercooling degree has a remarkable effect on nucleation rate. At 800 K, the Avrami exponent n has a value of 5.84(>4), which indicates an increasing nucleation rate with cooling time. As temperature decreasing to 750 K, the value of n =3.62 (<4) denotes a decreasing nucleation rate with cooling time. Especially at 700 K, the initial saturated nuclei and much higher supercooling degree block the succedent nucleation rate and result in a high ratio of grain boundary network, which is consistent with above analysis of atomic configuration energy.

Corresponding to the description of systematic ordering, the time evolution of local atomic structure and some characteristic bonded pairs from CNA are shown in Fig. 24. The three-staged process of crystallization is well reproduced in the evolution of local atomic structure. The enhancement of crystalline atoms mainly focuses on the stage of rapid growth. In addition, with the development of crystallization, the HCP-type atoms with laminar arrangement occupy a considerable proportion. This is because the FCC and HCP atoms have similar close-packed structure with tiny difference of atomic configurational energy. In the variation of bonded pairs, the change in the stage of nucleation is imperceptible. After the rapid growth of nuclei, the bonded pairs (421) become predominant, with its fraction achieving more than 60%. On the contrary, the relative numbers of the typical bonded pairs (433) and (544) only contribute to 5% of the total number of bonded pairs respectively, and the (555) almost disappear. Once a stable nucleus formed in supercooled liquid, the sample exhibited rapid growth of nuclei. This is the so-called instability for supercooled liquid relative to solid state.

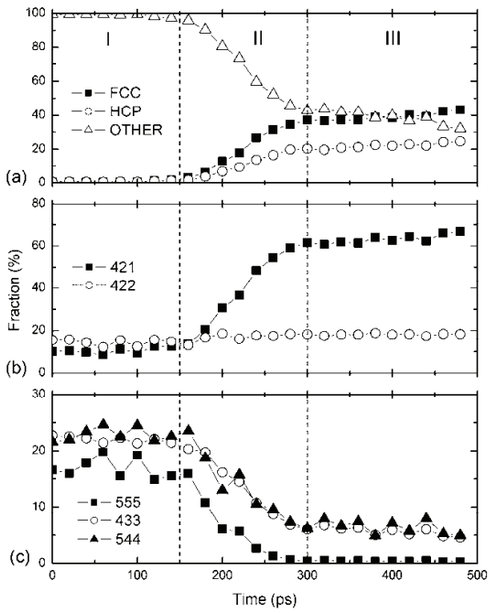

Fig. 24. The time evolution of local atomic structure and some characteristic bonded pairs from CNA in the course of crystallization at 800 K. (Picture redrawn from Ref. 74)

Different from conventional liquid, the nano-sized droplet exhibits particular freezing behavior. The investigation of gold nanoclusters revealed that ordered nanosurfaces with a

fivefold symmetry were formed with interior atoms remaining in the disordered state and the crystallization of the interior atoms that proceeded from the surface towards the core region induced an icosahedral structure.[75] While Bartell et al. found that when molten particles in a given series were frozen, several different final structures were obtained even though conditions had been identical.[76] Due to the structural diversity for small sized nanoparticles, the freezing behavior of nanodroplets present size dependence. Using MD simulation and local atomic structure analysis technique, we have investigated the freezing behavior of Ag nano-droplets with diameters ranging from 2 nm to 14 nm.

Figure 25 shows the freezing temperature with droplet size. In order to discuss the crystallization kinetics, the supercooling temperature relative to melting temperature of same sized nanoparitcles is shown in Fig. 25. Same as size-dependent melting temperature of nanoparticles, it is found that for Ag nano-droplets, their freezing temperature decreases with droplet size. But for the three small sized samples, their freezing temperature have the same value of 790±10 K. While the droplet size increases to a certain value, the freezing temperature of droplet even higher than that of conventional liquid despite the melting temperature of nanoparticle being lower than conventional materials. These are because on the nanoscale, the freezing temperature of droplet is affected not only by melting temperature, but also by the different freezing mechanism resulting from surface effect. According the classic nucleation theory, the homogeneous nucleation in conventional liquid originates from the interior and the required supercooling temperature generally is 0.2 T_m. However, we found that in our simulation, the nucleation for all sized samples is on the surface of nano-droplet. This results the deviation of effective supercooling temperature of nano-droplets from classic rule.

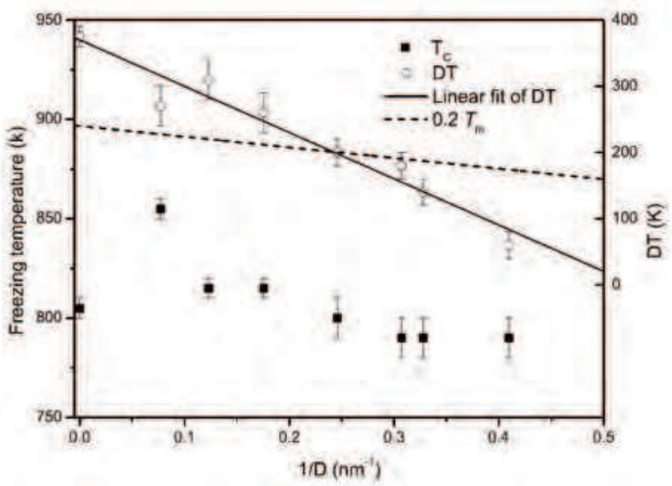

Fig. 25. The freezing temperature of Ag nano-droplt varying with droplet size.

According to the analysis of local atomic structure, Fig. 26 shows the freezing evolution for the sample of 2123 atoms. We can see that the crystalline nucleus first occurs on the surface layers of nano-droplet and with the preferential surface growth, the nano-droplet frozen into a particle with icosahedral structure.

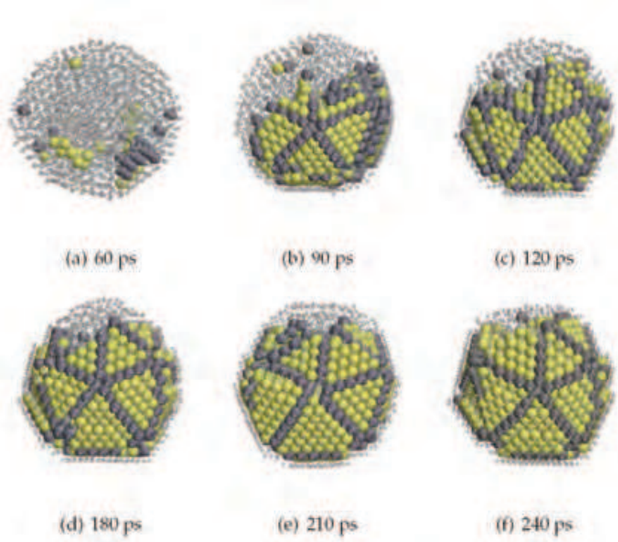

Fig. 26. The structural evolution in the course of freezing of the Ag nano-droplet with 2123 atoms, the yellow and black spheres represent the atoms with local FCC and HCP structure, respectively, the other atoms are denoted by star symbol.

5. Thermodynamic properties of alloy nanoparticles

In contrast to homogeneous nanoparticles composed of only one type of atom, the alloy nanoparticles exhibit more complicated structure and some special physical or chemical properties as a result of alloying effect. For instance, the Ag-Ni and Ag-Cu nanoparticles are of the core-shell structure with an inner Ni or Cu core and an Ag external shell,[77] and the Cu-Au nanoalloy clusters show an evident compositional dependence of structural characteristic.[78] Aguado et al. found that Li and Cs-doped sodium clusters have lower T_m than those of pure sodium ones for introducing a chemical defect.[79] However, a single Ni or Cu impurity in Ag icosahedral clusters considerably increases the T_m even for sizes of more than a hundred atoms.[80] Recently, the enhanced and bifunctional catalytic properties of bimetallic nanoparticles have made them attractive in the field of chemical catalysis.[81]
Driven by the high surface-to-volume ratio and surface free energy, the nanoparticles have a strong tendency of coalescence as they are put together. The molecular dynamics simulations has shown that the coalescence of iron nanoclusters occurs at the temperatures lower than the cluster melting point, and the difference between coalescence and melting temperatures increases with decreasing cluster size.[82] This feature are early expected to be applied in the alloying of components which are immiscible in the solid and/or molten state such as metals and ionics or metals and polymers.[83] As known from the Au-Pt alloy phase diagram, there exists a miscible gap for Au-Pt bulk alloy.[22] However, the Au-Pt alloy nanoparticles with several nanometers can be synthesized chemically almost in the entire composition range,[84] which demonstrates that the alloying mechanism and phase properties of nanoscale materials are evidently different from those of bulk crystalline state. For instance, Shibata et al. interpreted the size-dependent spontaneous alloying of Au-Ag

nanoparticles under the framework of defect enhanced diffusion.[85] By calculating the formation heat of Au-Pt nanoparticles from their monometallic ones using a thermodynamic model and analytic embedded atom method, we have analyzed size effect on the alloying ability and phase stability of immiscible binary alloy on a nanometer scale. It is of importance for the study of alloying thermodynamics of nanoparticles and the fabrication of immiscible alloys.[86]

According to the definition of formation heat being the energy change associated with the formation of alloy from its constituent substances, the formation heat of alloy nanoparticle from the pure nanoparticles of their constituents can be expressed as

$$E_f^{pA-B} = \frac{NE_c^{pA-B} - N(1-x)E_c^{pA} - NxE_c^{pB}}{N} \tag{16}$$

where the superscripts A-B, A and B denote alloy and its constituent elements A and B, respectively. N is the total number of atoms and x is the chemical concentration of element B in alloy nanoparticles. E_c^p is the mean atomic cohesive energy of nanoparticles. The size-dependent cohesive energy of nanoparticles has the following expression:[87]

$$E_c^p = E_c^b\left(1 - \frac{d}{D}\right) \tag{17}$$

where E_c^b is the cohesive energy of the corresponding bulk material. d and D represent the diameters of a single atom and nanoparticle respectively. For alloy nanoparticles, the d denotes the mean atomic diameter derived from Vegard's law. If neglecting the difference of atomic volume for atoms resided in the interior of and on the surface layer of nanoparticles, there exists a relation among d, D and the number of atoms (n) in a nanoparticle as follows.

$$\frac{d}{D} = \sqrt[3]{\frac{1}{n}} \tag{18}$$

Substituting Eq. 17 and 18 into Eq. 16 yields

$$E_f^{pA-B} = \frac{1}{N}\left[NE_c^{bA-B}\left(1 - \sqrt[3]{\frac{1}{N}}\right) - N(1-x)E_c^{bA}\left(1 - \sqrt[3]{\frac{1}{N(1-x)}}\right) - NxE_c^{bB}\left(1 - \sqrt[3]{\frac{1}{Nx}}\right)\right] \tag{19}$$

One can find that, to obtain the formation heat of alloy nanoparticle from the pure nanoparticles of its constituents, it is only needed to calculate the cohesive energy of the corresponding bulk alloy.

In order to calculate the composition-dependent cohesive energy of binary alloy, we adopted the MAEAM to describe the interatomic interactions.[88] For the interaction between alloy elements, we take the formula in Ref. 89. Thus, the cohesive energy of disordered solid solution can be written as

$$E_c^{bA-B} = \left(\frac{1}{2}\varphi^A + F^A(\rho) + M^A(P)\right)(1-x) + \left(\frac{1}{2}\varphi^B + F^B(\rho) + M^B(P)\right)x \tag{20}$$

The pair potential between two different species of atom A and B is included in the terms of φ^A and φ^B. All the model parameters, determined from fitting physical attributes such as lattice parameter, cohesive energy, vacancy formation energy and elastic constants, for Au, Pt and Au-Pt intermetallic compound.[86] Figure 27(a) shows the formation enthalpy of Au-Pt disordered solid solution from the present model together with other calculated [90-92] and

experimental values [93]. The results have a good agreement with experiment and other calculations, which indicates that the present AEAM model is reliable.

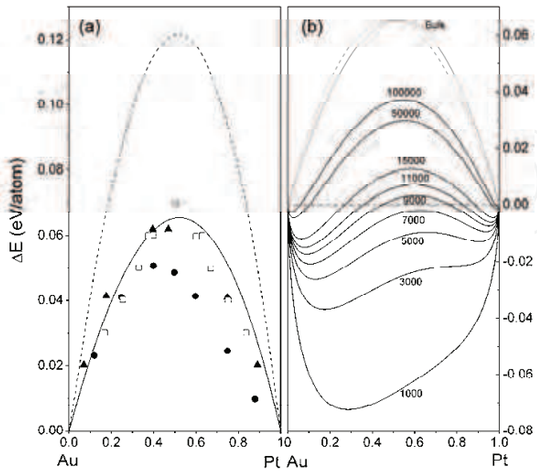

Fig. 27. (a) Formation heat for Au-Pt disordered solid solution as a function of Pt concentration. The solid line is the corresponding result from the present calculation; dash line and full circles present the results based on old EAM[90] and LMTO[91] respectively; open squares denote the calculation from Miedema theory[92]; full triangles denote the experimental data[93]. (b) The variation of the formation heat for Au-Pt nanoparticles of disordered structure along with Pt concentration at several indicated number of atoms in alloy nanoparticles. The dash line denotes mirror-image curve of that for bulk formation heat about the axis of x = 0.5, which give a clear comparison between the Au-Pt formation heat along with Au and Pt concentration. (Picture redrawn from Ref. 88)

Figure 27(b) shows the variation of formation heat of Au-Pt alloy nanoparticles with Pt atomic concentration for several samples with indicated total number of atoms (i.e. particle size). Naturally, as a result of alloying effect, the formation heat of alloy nanoparticles shows similar compositional dependence as in bulk materials. Comparing with bulk alloys, the most prominent characteristic on the formation heat of nanoparticles is its size-dependence. At a fixed Pt atomic concentration, the formation heat increases with the alloy particle size increasing, and its value even turns from negative to positive. This differs from the size-dependent formation enthalpy calculated by Liang et al.[94], where they only considered surface effect relative to the corresponding bulk materials. As the total number of atoms in Au-Pt alloy nanoparticles not exceeding 7 000 (about 6 nm in diameter of spherical particle), the formation heat within full concentration region is negative as a result of surface effect, which indicates that the alloying of Au and Pt nanoparticles becomes easy from the thermodynamic point of view, at the same time, indicates that the Au-Pt alloy nanoparticles within this size range having a better thermodynamic stability. In addition, the formation heat of bulk alloy has a great influence on that of nanoparticles. As shown in Fig. 27(b), the formation heat in Au-rich range for Au-Pt bulk alloy is lower than that in Pt-rich one. This difference is magnified in nanoparticles. Thus, in the Au-rich range, the Au-Pt nanoparticles show negative formation heat in a broad concentration range and a large particle size range, that is to say, the easy alloying region is extended. In Fig. 28, the contour of formation heat

of disordered Au-Pt nanoparticles is shown as a function of alloy nanoparticle size and the chemical concentration of Pt atom. For the nanoparticles with a dilute solute of Pt in Au or Au in Pt, there exists negative formation heat in a large particle size range. This can be looked as the instability of a small-size particle relative to a large one.

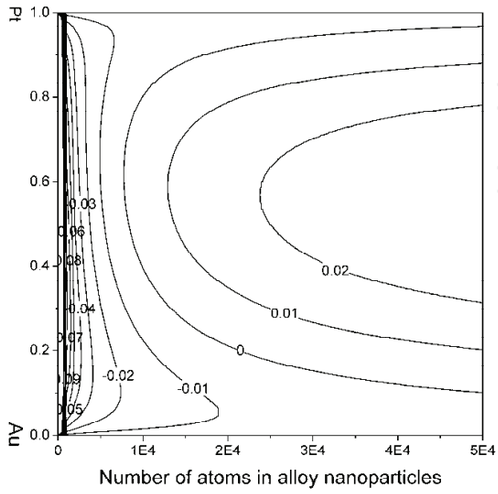

Fig. 28. The contour of formation heat for disordered Au-Pt nanoparticles as a function of alloy nanoparticle size and the chemical concentration of Pt atom. (Picture redrawn from Ref. 88)

As discussed above, the main difference between bulk material and nanoparticles is the surface effect of the latter. Figure 29 shows the changing of systematic surface area before and after alloying process under ideal condition (spherical nanoparticles without surface relaxation). Naturally, when the size of an alloy particle is fixed, there is a maximal difference of surface area for the alloying of two equal-volume monoatomic nanoparticles. Comparing Fig. 28 and 29, one can find that there is a maximal reduction in surface area after the alloying as Pt concentration is about 50%, but the formation heat is largest. This is because there exists a competition between surface effect and alloying effect on formation heat during alloying process for the immiscible nanoparticles.

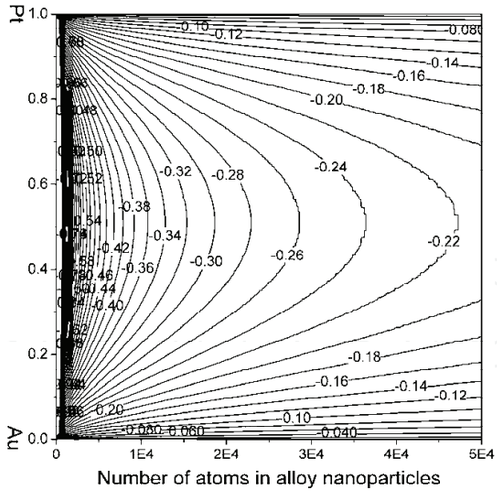

Fig. 29. The surface area changing contour of as a function of alloy nanoparticle size and the chemical concentration of Pt atom under the hypothesis of the disorered alloy obeying Vegard's law and the atoms in the interior of and on the surface of nanoparticle having the same volume. (Picture redrawn from Ref. 88)

In addition, since the Au has low surface energy (1.50 J/m^2) than that of Pt (2.48 J/m^2),[92] there is a thermodynamic driving force for Au atoms segregating to surface.[95] The segregation behavior in alloy nanoparticles generally induces the core-shell structure. Here we ignore the difference of structural details resulted by surface segregation. According to the effect of surface segregation being decreasing the systematic free energy, simply, a segregation factor f_{seg} is introduced to describe the changing of cohesive energy by surface segregation, i.e.

$$E_c^{bA-B}(Segregation) = f_{seg} \cdot E_c^{bA-B}(Ideal) \tag{21}$$

Figure 30 shows the variation of formation heat for Au-Pt alloy nanoparticles with different f_{seg}. Comparing with the formation heat of ideal alloy nanoparticles as shown in Fig. 28, the effect of surface segregation is extending the size range of alloy nanoparticles with negative formation heat. As the segregation factor f_{seg} increases from 1.001 to 1.008, the size of alloy nanoparticle, with negative formation heat in an entire composition range, increases from about 7 nm to 14 nm (number of atoms from 10^4 to 10^5).

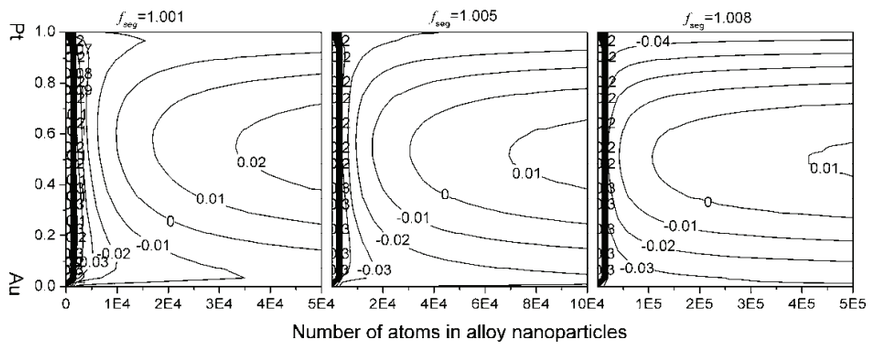

Fig. 30. The effect of surface segregation on the formation heat of alloy nanoparticles. (Picture redrawn from Ref. 88)

6. References

(1) H. Gleiter, Acta Mater. 2000, 48, 1.
(2) P. Pawlow, Z. Phys. Chem. 1909, 65, 1.
(3) M. Takagi, J. Phys. Soc. Jpn. 1954, 9, 359.
(4) F. Ding, K. Bolton, A. Rosen, J. Vac. Sci. Technol., 2004, A22, 1471.
(5) Y. Qi, T. Cagin,; W. L. Johnson, W. A. Goddard, J. Chem. Phys. 2001, 115, 385.
(6) P. Buffat, J. P. Borel, Phys Rev. 1976, A13, 2287.
(7) K. F. Peters, J. B. Cohen, Y. W. Chung, Phys. Rev. 1998, B57, 13430.
(8) C. L. Cleveland, W. D. Luedtke, U. Landman, Phys. Rev. Lett. 1998, 81, 2036.
(9) O. Gulseren, F. Ercolessi, E. Tosatti, Phys Rev. 1995, B51, 7377.
(10) K. K. Nanda, S. N. Sahu, S. N. Benera, Phys. Rev. 2002, A66, 013208.
(11) A. Safaei, M. A. Shandiz, S. Sanjabi, Z. H. Barber, J. Phys.: Condens. Matter 2007, 19, 216216.
(12) H. Reiss, P. Mirabel, R. L. Wetten, J. Phys. Chem. 1988, 92, 7241.
(13) J. G. Lee, H. Mori, Philos. Mag. 2004, 84, 2675.
(14) T. Tanaka, S. Hara, Z. Metallkd. 2001, 92, 467.
(15) J. B. Sturgeon, B. B. Laird, Phys Rev. 2000, B62, 14720.
(16) E. O. Arregui, M. Caro, A. Caro, Phys Rev. 2002, B66, 054201.
(17) W. H. Luo, W. Y. Hu, S. F. Xiao, J. Phys. Chem. 2008, C112, 2359
(18) H. Zhang, J. F. Banfield, J. Mater. Chem. 1998, 8, 2073.
(19) (a) J. W. Gibbs, In Collected Works; W. R. Longley, R. G. Van Name, Eds.; Longmans and Green: New York, 1931. (b) G. Wulff, Z. Kristallogr. 1901, 34, 449.
(20) H. Zhang, F. Huang, B. Gilbert, J. F. Banfield, J. Phys. Chem. 2003, B107, 13051.
(21) Z. H. Jin, K. Lu, Nanostruct. Mater. 1999, 12, 369.
(22) R. Hultgren, P. D. Desai, D. T. Hawkins, M. Gleiser, K. K. Kelly, D. D. Wagman, Selected Values of the Thermodynamic Properties of the Elements; American Society for Metals: Metals Park, OH, 1973.
(23) U. Hansen, P. Vogl, V. Fiorentini, Phys. Rev. 1999, B60, 5055.
(24) G. Grochola, S. P. Russo, I. K. Snook, I. Yarovsky, J. Chem. Phys. 2002, 116, 8547.
(25) G. Grochola, S. P. Russo, I. K. Snook, I. Yarovsky, J. Chem. Phys. 2002, 117, 7676.
(26) G. Grochola, S. P. Russo, I. K. Snook, I. Yarovsky, J. Chem. Phys. 2002, 117, 7685.

(27) L. Vitos, A. V. Ruban, H. L. Skriver, J. Kollar, Surf. Sci. 1998, 411, 186.
(28) W. R. W. A. Miller, Surf. Sci. 1977, 62, 267.
(29) V. K. Kumikov, K. B. Khokonov, J. Appl. Phys. 1983, 54, 1346.
(30) H. P. Bonzel, M. Nowicki, Phys Rev. 2004, B70, 245430.
(31) M. S. Daw, S. M. Foils, M. I. Baskes, Mater. Sci. Rep. 1993, 9, 251.
(32) (a) L. M. Holzman, J. B. Adams, S. M. Foils, W. N. G. Hitchon, J. Mater. Res. 1991, 6, 298. (b) B. Sadigh, G. Grimvall, Phys. Rev. 1996, B54, 15742. (c) M. Asta, D. Morgan, J. J. Hoyt, B. Sadigh, J. D. Althoff, D. de Fontaine, S. M. Foiles, Phys Rev. 1999, B59, 14271.
(33) L. E. Murr, Interfacial Phenomena in Metals and Alloys; Addison-Wesley: London, 1975.
(34) C. C. Yang, S. Li, Phys Rev. 2007, B75, 165413.
(35) F. Ercolessi, W. Andreoni, E. Tosatti, Phys. Rev. Lett. 1991, 66, 911.
(36) C. C. Yang, M. X. Xiao, W. Li, Q. Jiang, Solid State Commun. 2006, 139, 148.
(37) C. C. Yang, Q. Jiang, Acta Mater. 2005, 53, 3305.
(38) S. L. Lai, J. Y. Guo, V. Petrova, G. Ramanath, L. H. Allen, Phys. Rev. Lett. 1996, 77, 99.
(39) M. Y. Efremov, F. Schiettekatte, M. Zhang, E. A. Olson, A. T. Kwan, L. S. Berry, L. H. Allen, Phys. Rev. Lett. 2000, 85, 3560.
(40) E. A. Olson, M. Y. Efremov, M. Zhang, Z. Zhang, L. H. Allen, J. Appl. Phys. 2005, 97, 034304.
(41) V. N. Likhachev, G. A. Vinogradov, M. I. Alymov, Phys. Lett. A 2006, 357, 236.
(42) X. Li, J. J. Huang, Solid State Chem. 2003, 176, 234.
(43) H. Gleiter, Nanostruct. Mater. 1995, 6, 3.
(44) H. V. Atkinson, Acta Metall. 1988, 36, 469.
(45) P. G. Shewmon, Transformation in metals, McGraw-Hill, New York, 1969, pp. 300-306.
(46) A. J. Haslam, S. R. Phillpot, D. Wolf, D. Moldovan, H. Gleiter, Mater. Sci. Eng. 2001, A318, 293.
(47) N. Bernstein, Acta Mater. 2008, 56 1106.
(48) S. F. Xiao, W. Y. Hu, J. Crystal Growth 2006, 286,512
(49) K. E. Harris, V. V. Singh, A. H. King, Acta Mater. 1998, 46, 2623.
(50) D. Moldovan, V. Yamakov, D. Wolf, S. R. Phillpot, Phys. Rev. Lett. 2002, 89, 206101.
(51) P. Stoltze, J. Chem. Phys. 1990, 92, 6306.
(52) K. F. Peters, Y. W. Chung, J. B. Cohen, Appl. Phys. Lett. 1997, 71, 2391.
(53) J. F. Lutsko, D. Wolf, S. R. Phillpot, S. Yip, Phys. Rev. 1989, B40, 2841.
(54) W. Y. Hu, S. F. Xiao, J. Y. Yang, Z. Zhang, Eur. Phy. J. 2005, B45, 547
(55) H. W. Sheng, K. Lu, E. Ma, Nanostr. Mater. 1998, 10, 865.
(56) S. F. Xiao, W. Y. Hu, J. Y. Yang, J. Phys. Chem. 2005, B109, 20339
(57) S. F. Xiao, W. Y. Hu, J. Y. Yang, J. Chem. Phys. 2006, 125, 184504
(58) T. Nguyen, P. S. Ho, T. Kwok, C. Nitta, S.Yip, Phys. Rev. Lett. 1986, 57, 1919.
(59) W. H. Qi, M. P. Wang, Mater. Chem. Phys. 2004, 88, 280.
(60) L. E. Murr, Interfacial Phenomena in Metals and Alloys; Addison Wesley: New York, 1975.
(61)J. Schiotz, K. W. Jacobsen, Science 2003, 301, 1357.
(62)K. Lu, Mater. Sci. Eng. Rep. 1996, 16, 161.
(63)Y. H. Zhao, K. Lu, T. Liu, Phys. Rev. 1999, B59, 11117.
(64)P. M. Derlet, H. van Swygenhoven, Phys. Rev. 2003, B67, 014202.
(65) U. Tartaglino, T. Zykova-Timan, F. Ercolessi, and E. Tosatti, Phys. Rep. 2005, 411, 291.

(66) C. S. Hsu, A. Rahman, J. Chem. Phys. 1979, 79, 5234.
(67) D. Moroni, P. R. ten Wolde, P. G. Bolhuis, Phys. Rev. Lett. 2005, 94, 235703.
(68) B. O'Malley, I. Snook, Phys. Rev. Lett. 2003, 90, 085702.
(69) J. M. Leyssale, J. Delhommelle, C. Millot, J. Chem. Phys. 2005, 122, 184518.
(70) C. S. Liu, J. Xia, Z. G. Zhu, D. Y. Sun, J. Chem. Phys. 2001, 114, 7506.
(71) M. Matsumodo, S. Saito, I. Ohmine, Nature 2002, 416, 409.
(72) P. Beaucage, N. Mousseau, Phys. Rev. 2005, B71, 094102.
(73) J. M. Leyssale, J. Delhommelle, C. Millot, J. Chem. Phys. 2005, 122, 104510.
(74) S. F. Xiao, W. Y. Hu, J. Chem. Phys. 2006, 125, 014503
(75)W. A. Johnson, R. F. Mehl, Trans. Am. Inst. Min. Metall. Pet. Eng. 1939, 135, 416.
(76)M. Avrami, J. Chem. Phys. 1939, 7, 1103; 1940, 8, 212.
(77) H. S. Nam, Nong M. Hwang, B. D. Yu, J. K. Yoon, Phys. Rev. Lett. 2002, 89, 275502.
(78) Y. G. Chushak, L. S. Bartell, J. Phys. Chem. 2001, B105, 11605.
(79) G. Rossi, A. Rapallo, C. Mottet, A. Fortunelli, F. Baletto, R. Ferrando, Phys. Rev. Lett. 2004, 93, 105503.
(80) S. Darby, T. V. Mortimer-Jones, R. L. Johnston, C. Roberts, J. Chem. Phys. 2002, 116, 1536.
(81) A. Aguado, L. E. Gonzalez, J. M. Lopez, J. Phys. Chem. 2004, B108, 11722.
(82) C. Mottet, G. Rossi, F. Baletto, R. Ferrando, Phys. Rev. Lett. 2005, 95, 035501.
(83) S. Koutsopoulos, K. M. Eriksen, R. Fehrmann, J. Catal. 2006, 238, 270.
(84) F. Ding, A. Rosen, K. Bolton, Phys. Rev. 2004, B70, 075416.
(85) R. Birringer, Mater. Sci. Eng. 1989, A117, 33.
(86) J. Luo, M. M. Maye, V. Petkov, N. N. Kariuki, L. Wang, P. Njoki, D. Mott, Y. Lin, C. J. Zhong, Chem. Mater. 2005, 17, 3086.
(87)T. Shibata, B. A. Bunker, Z. Zhang, D. Meisel, C. F. Vardeman II, ; J. D. Gezelter, J. Am. Chem. Soc. 2002, 124, 11989.
(88) S. F. Xiao, W. Y. Hu, W. H. Luo, Y. R. Wu, X. F. Li, H. Q. Deng, Eur. Phys. J. 2006, B54, 479.
(89)W. H. Qi, M. P. Wang, J. Mater. Sci. Lett. 2002, 21, 1743.
(90)J. Y. Yang, W. Y. Hu, H. Q. Deng, D. L. Zhao, Surf. Sci. 2004, 572, 439.
(91)Y. R.Wu, W. Y. Hu, S. C. Han, J. Alloy Comp. 2006, 420, 83.
(92)R. A. Johnson, Phys. Rev. 1990, B41, 9717.
(93)I. A. Abrikosov, H. L. Skriver, Phys. Rev. 1993, B47, 16532.
(94)F. R. De Boer, R. Boom, W. C. M. Mattens, A. R. Miedema, A. N. Niessen, Cohesion in Metals; North-Holland: Amsterdam, 1988.
(95)H. J. Schaller, Z. Metallkde 1979, 70, 354.
(96)L. H. Liang, G. W. Yang, B. Li, J. Phys. Chem. 2005, B109, 16081.
(97)T. T. Tsong, Y. S. Ng, S. B. McLane, J. Chem. Phys. 1980, 73, 1464.

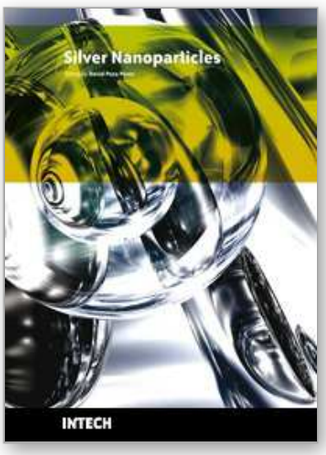

Silver Nanoparticles

Edited by David Pozo Perez

ISBN 978-953-307-028-5
Hard cover, 334 pages
Publisher InTech
Published online 01, March, 2010
Published in print edition March, 2010

Nanotechnology will be soon required in most engineering and science curricula. It cannot be questioned that cutting-edge applications based on nanoscience are having a considerable impact in nearly all fields of research, from basic to more problem-solving scientific enterprises. In this sense, books like “Silver Nanoparticles” aim at filling the gaps for comprehensive information to help both newcomers and experts, in a particular fast-growing area of research. Besides, one of the key features of this book is that it could serve both academia and industry. “Silver nanoparticles” is a collection of eighteen chapters written by experts in their respective fields. These reviews are representative of the current research areas within silver nanoparticle nanoscience and nanotechnology.

InTech Europe
University Campus STeP Ri
Slavka Krautzeka 83/A
51000 Rijeka, Croatia
Phone: +385 (51) 770 447
Fax: +385 (51) 686 166
www.intechopen.com

InTech China
Unit 405, Office Block, Hotel Equatorial Shanghai
No.65, Yan An Road (West), Shanghai, 200040, China
中国上海市延安西路65号上海国际贵都大饭店办公楼405单元
Phone: +86-21-62489820
Fax: +86-21-62489821

IntechOpen